

QUANTITATIVE ANALYSIS OF 2D ELECTRONICALLY SCANNING POLARIMETRIC PLANAR PHASED ARRAY RADAR MEASUREMENTS

Junho Ho^{a,b}, Guifu Zhang^{a,b}, Zhe Li^c, Petar Bukovcic^{d,e}, Alexander Ryzhkov^{d,e}, Jidong Gao^e, Jacob T. Carlin^{d,e}, and Jeffrey C. Snyder^e

^a School of Meteorology, University of Oklahoma, Norman, Oklahoma, USA

^b Advanced Radar Research Center, University of Oklahoma, Norman, Oklahoma, USA

^c MathWorks, Natick, Massachusetts, USA

^d Cooperative Institute for Severe and High-Impact Weather Research and Operations, University of Oklahoma, Norman, Oklahoma, USA

^e NOAA/OAR National Severe Storms Laboratory, Norman, Oklahoma, USA

1. INTRODUCTION

Phased array radars (PARs) are an emerging technology in the meteorological community. They offer the advantage of providing rapid and timely information that greatly enhances the understanding of severe weather phenomena as they unfold (Kuster et al., 2016; Wilson et al., 2017). PARs are also versatile and can effectively serve multiple purposes (Zrnic et al., 2007; Zhang and Doviak, 2007; Heinselman et al., 2008; Stailey and Hondl, 2016; Kollias et al., 2022). Many countries are actively involved in developing PAR systems to replace or complement existing dish-based operational radars (e.g., Kollias et al., 2022; Palmer et al., 2022).

In recent years, digital beamforming methods have been introduced to enhance multi-functional flexibility (Stailey and Hondl, 2016), adaptive beamforming (Wirth, 2013; Fulton et al., 2016), and space-time adaptive processing (Melvin, 2004) in 2D PARs, with electronic steering in both azimuth and elevation. However, there are unique challenges with using 2D PARs for meteorological purposes that have been discussed in the literature (e.g., Zhang et al. 2009), including the complexity of providing high-quality polarimetric measurements. An S-band fully digital PPPAR, named Horus, was developed by the Advanced Radar Research Center at the University of Oklahoma (OU) with funding from the National Severe Storms Laboratory (NSSL) and the Office of Naval Research (Palmer et al., 2023). The fully digital design, with element-level analog to digital converters, can provide numerous advantages, including high flexibility in spatio-temporal resolution and sampling, beam agility, interference mitigation, and, in theory, software configurability. However, as a 2D PPPAR, Horus faces challenges in calibrating polarimetric variables to meet the requirements for weather observation (Zhang et al., 2009; Zhang et al., 2011; Lei et al., 2015; Palmer et al., 2023).

Challenges affecting data quality of 2D PPPAR include geometrically induced cross-polarization coupling and sensitivity loss (Zhang et al., 2011; Zhang, 2016).

PPPARs use hundreds of beams with different characteristics, which require beam steering-dependent calibration (Ivic et al. 2019; Weber et al., 2021). The most critical concern is the loss of sensitivity when steering at wide angles off-broadside; while the bias can be corrected, the loss of sensitivity and purity is difficult to recover and may require increased antenna size and higher transmit power to meet sensitivity requirements at large off-broadside angles (Zhang et al., 2011). Recently developed calibration methods show promise for mitigating such problems (e.g., Fulton et al., 2022). Nevertheless, the complexity of 2D PPPAR polarimetric calibration remains due to calibration procedures required for each element and direction.

The primary objective of this study is to analyze the error statistics of the weather observations to assess the quality of the polarimetric data in its current state and to identify any potential system deficiencies. The present results can be valuable in further guiding the system development process and post-processing techniques for meteorological applications.

2. DATA AND ERROR CALCULATIONS

a. Horus experiment configurations

The Horus radar system has a planar design with 5 × 5 panels, each panel consisting of 8 × 8 dual-polarization antenna elements. Its full aperture size is 2.03 m × 2.03 m, and it operates at the S-band at approximately 3.07 GHz (Table 1). For this study, two sets of measurements are examined from when the radar was configured with 5 and 13 out of 25 panels, with transmit powers of 3.2 and 8.32 kW, respectively (Fig.1). When going from 5 to 13 panels, the antenna gain increased from 26.5 dB to 31.5 dB, while the half-power beamwidth decreased from approximately 13° to 3.3° in azimuth and remained at 3.3° in elevation, respectively. Currently, only range-height indicator (RHI) scans have been performed with 63 and 64 elevation angles for 5 and 13 panels, respectively. A total of eight cases have been measured by Horus, with six cases occurring prior to August 2023 using 5 panels and two subsequent cases using 13 panels. The scanning range resolution was 19.2 m from the progressive pulse compression technique (Salazar Aquino et al., 2021), and the temporal resolution was approximately 2 to 4 seconds depending on the pulse repetition time of 0.5 to 1 ms with 64 samples per dwell. The scanning strategy with the 13-panel update

* Corresponding author address: Junho Ho, Univ. of Oklahoma, School of Meteorology, Norman, OK 73072; e-mail: jhho0626@ou.edu

consists of a mechanical inclination of 2° and electronic scanning of 64 elevation angles between 0° and 31.5° at 0.5° intervals, or an inclination of 33.5° with scans ranging from -31.5° to 31.5° in elevation (i.e., ~ 2 to 65° ground-relative elevation angles) at 1° intervals.

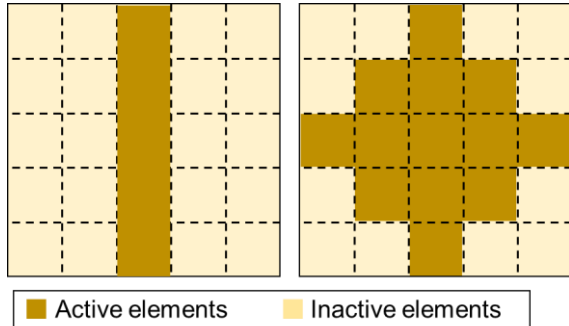


Figure 1. Depiction of the active elements used for 5- and 13-panel measurements. The dark yellow denotes the active elements, and the lighter yellow inactive elements.

Radar Parameters	5 panel Horus	13 panel Horus	KTLX
Frequency (GHz)	3.07	3.07	2.8
Transmit power (kW/polarization)	3.2	8.32	375
Antenna gain (dB)	26.5	31.5	45.5
Elevation beamwidth ($^\circ$)	3.3	3.3	0.925
Azimuth beamwidth ($^\circ$)	13	3.3	0.925

Table 1. Specifications of Horus with 5 and 13 panels, and KTLX.

b. Reference measurements and error statistics calculations

The reconstructed RHI KTLX beams do not exactly match the Horus RHI because the systems are not co-located and the beamwidths of the two radars are much different. The reconstructed KTLX RHI was formed over the Horus measurement plane for comparison to quantify the mean bias and standard deviation. In order to minimize differences, each elevation and time were carefully matched by selecting the Horus rays from the best-matching KTLX observation time for each elevation angle. The time can be well matched in the case of Horus and KTLX because Horus provides 2 to 4-second updates. Note that nearest-neighbor interpolation was used for both the KTLX reconstructed RHI and the gridded Horus data. The KTLX reconstructed RHI were converted to match the Horus RHI scans for easier error quantification in the subsequent analyses. It should be noted that, even beyond the aforementioned matching in time and space, inherent mismatches persist between the interpolated RHIs due to differences in radar resolution, beam width, and location.

The standard deviation calculation for polarimetric radar measurements has traditionally been performed using spatial sampling assuming homogeneous precipitation field, typically employing $2R+1$ range gates, as demonstrated in an earlier CPPAR data

analysis with $R = 5$ (Li et al., 2021) and shown in Equation (1),

$$\text{STD}(X) = \sqrt{\frac{1}{2R+1} \sum_{m=i-R}^{i+R} (X_m - \bar{X})^2}, \quad (1)$$

where i is the gate number at which the standard deviation is estimated, and X_m is the polarimetric data at gate m and \bar{X} the mean value of consecutive $2R+1$ gates from $m = i-R$ to $m = i+R$.

Rather than spatial sampling, given the assumptions of ergodicity and local stationarity that apply to the Horus data due to its rapid updates every 2 to 4 seconds, it is possible to compute the standard deviation of the radar data from temporal samples. This approach involves examining the differences between successive time steps over the entire dataset. Since different range gates observe distinct parts of the precipitation field, and the movement of storms within 4 seconds generally falls within the range resolution, using temporal samples can provide more accurate estimates in many cases, since one does not have to assume spatial homogeneity. The standard deviation is calculated for various polarimetric variables, including Z_H , velocity (v_r), spectrum width (σ_v), Z_{DR} , ρ_{hv} , and differential phase shift (Φ_{DP}), for both spatial and temporal sampling. In the spatial sampling approach, 11 range gates were used to calculate the standard deviation and were averaged over 127 time steps. Experimenting with different time steps or increasing the number of samples did not significantly change or improve the standard deviations. The 127 temporal samples selected after removing abnormal time steps/strips were used to calculate the standard deviation using Equation (2),

$$\text{STD}(X) = \sqrt{\frac{1}{2(N-1)} \sum_{n=1}^{N-1} |(X_{n+1} - X_n)|^2} \quad (2)$$

where N is the number of temporal samples, X_{n+1} is the polarimetric variables at t_{n+1} and X_n at t_n . The computed values for both spatial and temporal samples are compared to theoretical values and the radar functional requirements set by the National Oceanic and Atmospheric Administration/National Weather Service (NOAA/NWS RFR). The theoretical values were derived using equations from Doviak and Zrnica (2006).

3. COMPARISON AND VALIDATION OF HORUS DATA

Before entering into the discussion of error statistics, it is essential to acknowledge the data filtering and processing applied to the Horus measurements prior to the error statistic calculations. Various filters were employed, including a clutter filter (Siggia and Passarelli, 2004), a radio frequency interference filter (Cho, 2017), and a noise estimator (Ivic et al., 2013). These filtering techniques can noticeably influence the standard deviation calculation, especially when dealing with spatial samples. Furthermore, an adaptive multi-lag estimator was used for Horus. This approach uses lag-0 for SNR above 15 dB and various combinations of lags 0, 1, 2, and 3 for lower SNR ranges (Lei et al.,

2012; Warde et al., 2023). This adaptive multi-lag estimator, along with the applied filters, may potentially affect the calculated standard deviations from spatial and temporal samples.

a. 5-panel measurement

Horus began its first weather observations in December 2022 and continues to observe instances of shallow and deep convective precipitation. This study specifically examines a recent convective precipitation event that occurred on 11 May 2023, from 23:50 to 01:20 UTC the following day. The Norman sounding taken at 0000 UTC 12 May 2023 revealed favorable environmental conditions for deep convective storms, with convective available potential energy (CAPE) of $\sim 2700 \text{ J kg}^{-1}$. Remnants of outflow boundaries from morning convection, surface heating, and low-level moisture advection provided sufficient lift for deep moist convection to form. The strong mid-level winds provided sufficient shear for supercell formation. The convective cell of interest originated near the southwestern Oklahoma/northwestern Texas border around 21:45 UTC, and a band of supercells embedded in a loosely organized mesoscale convective system moved across Oklahoma. According to the NWS, numerous reports of tornadoes and hail were documented throughout central and southwestern Oklahoma (<https://www.spc.noaa.gov/exper/archive/event.php?date=20230511>). As illustrated in Fig. 1, the Horus beam was directed at an azimuth of 270 degrees from the north, penetrating the convective region of the storm.

i) Horus-KTLX comparison

The spatial distribution of polarimetric variables from the two radars shown in Fig. 2 provides valuable information to identify potential system deficiencies and to understand the error characteristics of Horus. KTLX, which benefits from higher antenna gain and transmit power, exhibits significantly higher SNR compared to Horus. The Horus and KTLX data are relatively well-matched in time and space, although differences due to interpolation can still be observed. Overall, the convective core and stratiform patterns demonstrate good agreement. However, some discrepancies in the magnitude of certain measurements exist. For example, the maximum Z_H near the ground, at about 37 km, exhibits a difference of about 5 dBZ. In addition, many of the weak echoes below 5 dBZ from KTLX are not present in the Horus measurements due to differences in sensitivity.

Z_{DR} for Horus shows a significant bias near the ground, which is likely influenced by clutter contamination due to the relatively large beamwidth (Fig. 2). Z_{DR} values from Horus are about 3 to 4 dB below 4 km AGL, while KTLX has values of ~ 2.5 dB near the ground. It is noted that KTLX has limited observations at the lower elevations due to its distance from the storm, and the near-ground data are extrapolated from higher altitudes. While the biases in

Z_H and Z_{DR} may seem rather large, it should be noted that KTLX measurements may also contain biases. The error statistics of ρ_{hv} are typically utilized to assess the system performance. The ρ_{hv} from Horus also shows smaller values in the lower elevations with 0.9 to 0.94 below ~ 1 km AGL and in regions of lower SNR. While standard deviations can be mitigated relatively easily by additional filtering, ρ_{hv} biases are especially difficult to remove and can have negative effects in meteorological applications. Satisfying the bias specified in the radar functional requirements is essential to improve the accuracy and reliability of the measurements.

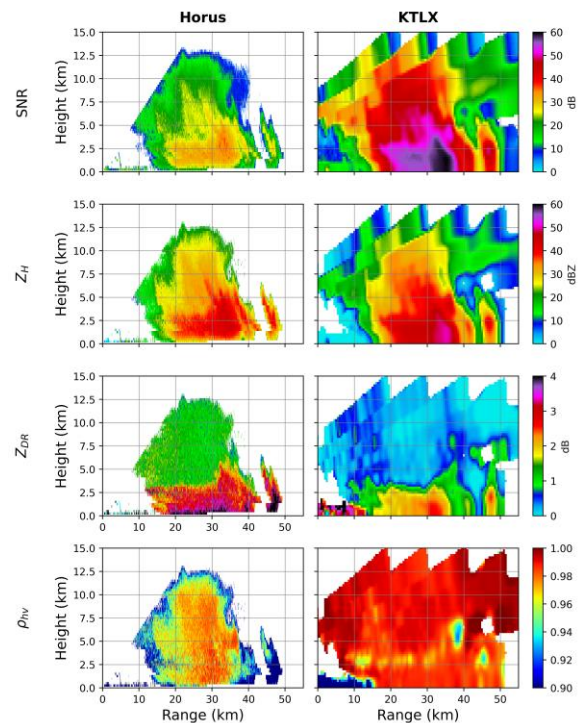


Figure 2. Spatial distribution of SNR, Z_H , Z_{DR} , and ρ_{hv} from Horus and KTLX measurements. The polarimetric variables are plotted for SNR larger than 10 dB.

The mean bias and standard deviation of the differences between Horus and KTLX are presented in Table 2 for various SNR thresholds. The mean bias and standard deviation of the Z_H from Horus remain relatively stable and consistent across different SNR ranges, due to the availability of a sufficient number of samples. The bias in Z_{DR} increases slightly with SNR, but the mean bias stays close to 0.9 dB. The standard deviations for Z_H and Z_{DR} are also consistent, ranging from 6.92 to 6.09 dB and from 0.79 to 0.64 dB, respectively. The standard deviation values are comparable or larger than the corresponding mean bias values, suggesting that beam broadening or mismatch may have some effect on these statistics. The negative bias of ρ_{hv} persists, even after removing the two lowest elevations. However, as clutter and non-meteorological echoes are progressively removed with higher SNR, the mean bias gradually decreases. This

trend indicates an improvement in the accuracy of ρ_{hv} measurements with increasing SNR.

(a) Mean bias

	0≤SNR	5≤SNR	10≤SNR	15≤SNR	20≤SNR
Z_H (dBZ)	-2.79	-2.79	-3.06	-3.24	-3.44
Z_{DR} (dB)	0.87	0.87	0.9	0.93	0.96
ρ_{hv}	-0.012	-0.012	-0.009	-0.006	-0.003

(b) Standard deviation

	0≤SNR	5≤SNR	10≤SNR	15≤SNR	20≤SNR
Z_H (dBZ)	6.92	6.92	6.6	6.12	6.09
Z_{DR} (dB)	0.79	0.79	0.71	0.64	0.64
ρ_{hv}	0.047	0.047	0.028	0.016	0.014

Table 2. Table of the mean and standard deviation for the differences between Horus and KTLX for each SNR range.

ii) Standard deviation calculations

While the standard deviations in Table 2b were calculated from the differences between Horus and KTLX, the subsequent Horus standard deviations are calculated using spatial and temporal samples (Table 3). Thus, the standard deviations of v_r and Φ_{DP} are included in Table 3 as they are transmission and/or location dependent. The calculated standard deviations for each signal-to-noise ratio (SNR) range, theoretical values, and the NOAA/NWS RFR are organized in Table 3, based on spatial (Table 3a) and temporal (Table 3b) sampling. Similar to the KTLX comparison, the standard deviation of the polarimetric variables generally exhibits a decreasing trend with increasing SNR. However, for larger SNR ranges, slight fluctuations are expected due to the smaller number of available data points. Given SNR values above 20 dB, the standard deviations for all variables are even smaller than the theoretical calculations. Most variables exceed the theoretical values even for SNR larger than 0. This could be attributed to the influence of post-processing filters, especially when dealing with spatial samples. The use of lag-0 assumptions in the calculation of the theoretical values may also play a role, considering multi-lag estimators are used in the data processing. In addition, there are large differences in the standard deviations between spatial and temporal samples, especially in the lower SNR regions. For instance, the standard deviations of Z_H in the SNR range from 5 to less than 20 dB are about twice as large as for the temporal samples, while Z_{DR} and Φ_{DP} show larger standard deviations for the spatial samples. These results clearly highlight the influence of spatial averaging by the filters and emphasize the need to account for this in subsequent analyses. Nevertheless, the standard deviation for SNR values greater than 20

dB agrees well with the theoretical predictions and is comparable to the NOAA/NWS RFR limits.

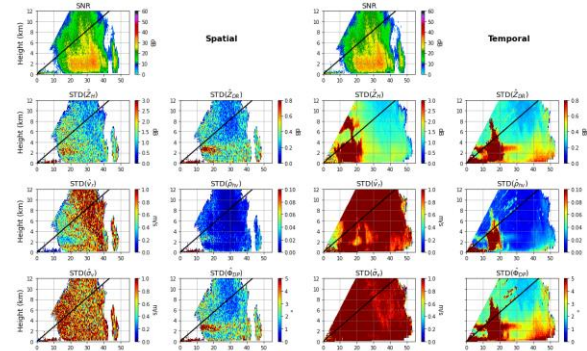


Figure 3. Spatial distribution of SNR, and standard deviations of reflectivity (Z_H), radial velocity (v_r), spectrum width (σ_v), differential reflectivity (Z_{DR}), correlation coefficient (ρ_{hv}), and differential phase shift (Φ_{DP}) from Horus weather observations on 11 May 2023. The left column is based on spatial samples using 11 gates, and the right temporal.

Examples of the spatial distribution of the standard deviations for each polarimetric variable are depicted in Fig. 3. Horus used non-linear frequency modulations with a pulse width of 80 μ s and a bandwidth of 5 MHz, and the blind range was mitigated by a progressive pulse compression technique (Salazar Aquino et al., 2021). However, larger standard deviations are expected in the removed blind range of \sim 12 km. Due to the effects of clutter and contamination, the standard deviations for all variables from Horus have large values in the near-range region. Notably, the convective core regions characterized by high SNR tend to have lower standard deviation values. Both v_r and σ_v show high values throughout, with relatively lower values behind and in front of the convective region for temporal samples. As expected, Horus displays larger standard deviations in Z_{DR} , ρ_{hv} , and Φ_{DP} at around 3 km height between 10 and 20 km near the melting level. Overall, the standard deviation values in Fig. 3 exhibit reasonable distributions, consistent with the results in Table 3.

(a) Spatial

	0≤SNR	5≤SNR<10	10≤SNR<15	15≤SNR<20	20≤SNR	Theory	NOAA/NWS RFR
Z_H (dBZ)	0.96	0.55	0.59	0.54	0.82	1.03	1.8
v_r (m/s)	0.80	0.54	0.54	0.57	0.79	1.3	1.0
σ_v (m/s)	0.90	0.91	0.59	0.49	0.70	1.32	1.0
Z_{DR} (dB)	0.33	0.34	0.25	0.19	0.21	0.38	0.3
ρ_{hv}	0.024	0.033	0.014	0.007	0.006	0.008	0.006
Φ_{DP} (°)	2.57	3.00	1.82	1.29	1.40	2.08	2.0

(b) Temporal

	0≤SNR	5≤SNR<10	10≤SNR<15	15≤SNR<20	20≤SNR	Theory	NOAA/NWS RFR
Z_H (dBZ)	1.22	0.92	0.95	0.91	1.09	1.03	1.8
v_r (m/s)	1.07	0.95	0.98	1.07	1.20	1.3	1.0
σ_v (m/s)	1.13	1.46	0.95	0.84	0.94	1.32	1.0

Z_{DR} (dB)	0.44	0.54	0.39	0.30	0.32	0.38	0.3
ρ_{hv}	0.031	0.054	0.022	0.011	0.01	0.008	0.006
Φ_{DP} (°)	3.30	4.70	2.78	2.02	2.12	2.08	2.0

Table 3. The standard deviation of six moments based on both (a) the spatial and (b) the temporal domain of the Horus data for five different signal-to-noise ratio (SNR) ranges. The NOAA/NWS RFR represent the radar functional requirements of NOAA and the National Weather Service.

b. 13-panel measurement

Since the 13-panel update in August 2023, Horus has continued to collect weather observations of deep convective events. This part of the study focuses on the second collected event on 4 October 2023 from 22:19 to 22:45 UTC, with the primary attention given to the period between 22:36 and 22:45 UTC. The 1800 UTC 4 October 2023 Norman sounding shows a CAPE of $\sim 3078 \text{ J kg}^{-1}$. With the combination of abundant low-level moisture, diurnal boundary layer heating, and an approaching mid-level shortwave trough, favorable conditions for thunderstorm development were present. The group of isolated convective cells of interest originated near the western Oklahoma/northwestern Texas border around 17:50 UTC, and a mesoscale convective system moved across Oklahoma. Several reports of severe winds and hail were documented across central and northeastern Oklahoma (<https://www.spc.noaa.gov/exper/archive/event.php?date=20231004>). Horus utilized two different scanning strategies at two different azimuth angles. This analysis will mainly focus on the first scanning strategy for better comparison with KTLX. The Horus beam of the first scanning strategy was directed at an azimuth of 198° from the north (i.e., to the south-southwest), penetrating the convective region of the storm.

i) Comparison with KTLX

The convective core located between 10 and 25 km demonstrates good agreement between the radars (Fig. 4). However, there are still some clear differences in the magnitude of the measurements. For example, the maximum Z_H near the ground, at about 15 km, exhibits a difference of more than 5 dB, and a lack of sensitivity in the Horus data remains apparent at further distances. Despite the bias, Horus's ability to capture true RHIs provides much more detailed microphysics and dynamical process information due to the improved data coverage, demonstrating the potential of PARs to improve meteorological applications. The Z_{DR} bias is not as evident as the 5-panel case, with no notable location of significant bias and minimal difference near the convective core (Fig. 4). Overall, the Z_{DR} values from Horus agree well with KTLX, with positive biases of less than 0.5 dB throughout the entire domain. Note that KTLX has limited observations at the lower elevations due to its distance from the storm, and the near-ground data are interpolated from higher altitudes. The high ρ_{hv} in Horus is notable in the lower elevations, and the melting level agrees well with KTLX. However, Horus shows smaller

ρ_{hv} values of less than 0.9 in the mid-altitude regions from 2.5 to 7.5 km at low elevations, and they are more pronounced starting at a range of about 20 km. This is partly contributed by snow melt and unidentified sources of error related to electronic steering at large angles from the broadside. Future improvements in PPAR signal processing for weather applications are planned in light of the observed biases in the Z_{DR} and ρ_{hv} , and the need to minimize the influence of clutter and contamination by addressing beam width and steering loss issues.

(a) Mean bias

	0 \leq SNR	5 \leq SNR	10 \leq SNR	15 \leq SNR	20 \leq SNR
Z_H (dBZ)	4.46	4.46	4.66	4.99	5.45
Z_{DR} (dB)	0.28	0.28	0.27	0.26	0.25
ρ_{hv}	-0.009	-0.009	-0.01	-0.011	-0.009

(b) Standard deviation

	0 \leq SNR	5 \leq SNR	10 \leq SNR	15 \leq SNR	20 \leq SNR
Z_H (dBZ)	4.76	4.76	4.72	4.71	4.62
Z_{DR} (dB)	0.41	0.41	0.41	0.42	0.43
ρ_{hv}	0.046	0.046	0.047	0.047	0.045

Table 4. Mean and standard deviation of the differences between Horus and KTLX for each SNR range.

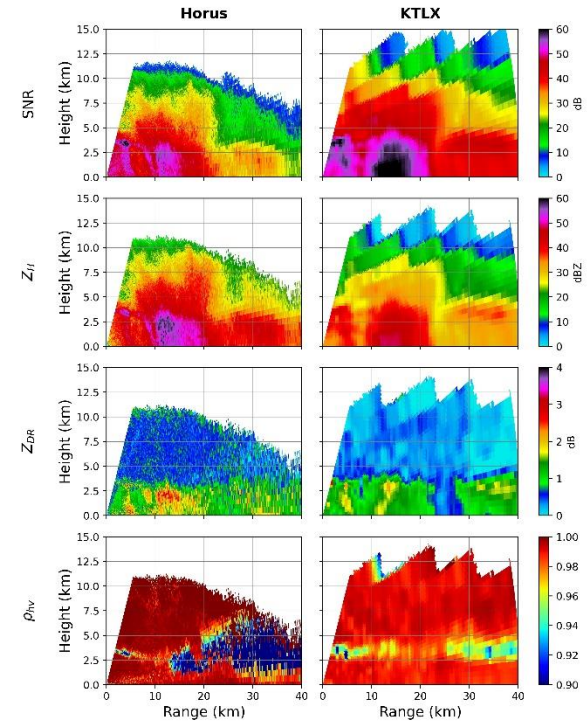


Figure 4. Spatial distribution of SNR, Z_H , Z_{DR} , and ρ_{hv} from Horus and KTLX measurements on October 4th, 2023. The polarimetric variables are plotted for SNR larger than 10 dB.

Compared to the 5-panel results, the mean bias and standard deviations from the KTLX comparison remain relatively stable and consistent across different SNR ranges (Table 4). The mean bias and standard deviations for Z_H are comparable, and Z_{DR} shows improvements over the 5-panel results, ranging from 4.46 to 5.45 dB and from 0.25 to 0.28 dB, respectively. Similar to the previous case, the standard deviation values are typically similar to or greater than the corresponding mean bias values, with limited influence of beam broadening or mismatch on these statistics. Also, there is minimal improvement in the accuracy of ρ_{hv} measurements with increasing SNR, suggesting that such a reduction is not due to lower SNR values. However, the consistently low ρ_{hv} bias even for the 13-panel results is of concern, especially for the significant ρ_{hv} reduction between 20 and 40 km.

ii) Standard deviations

Both the spatial and temporal standard deviations from Horus appear to be much smaller compared to those from the 5-panel configuration. For Z_H , higher standard deviation values up to 3 dB are observed based on temporal samples, but these are mostly filtered or smoothed in the spatial samples. The high standard deviation values are relatively evenly distributed beyond a range of 15 km (Fig. 5). In particular, the convective core regions characterized by high SNR tend to have lower standard deviation values. Horus shows more distinct regions with larger standard deviations of v_r from temporal samples near the convective region and at greater distances. The larger standard deviations of Z_{DR} , ρ_{hv} , and Φ_{DP} at around 3 km height between 0 and 12 km range are expected because the progressive pulse compression technique was applied to remove the blind range (Salazar Aquino et al., 2021). However, strips of increased standard deviation of Z_{DR} , ρ_{hv} , and Φ_{DP} are observed at low elevations may be related to the performance degradation. Additional analysis seems necessary to identify the potential cause. However, the majority of the data points fall below 0.3 dB, 0.01, and 3° for Z_{DR} , ρ_{hv} , and Φ_{DP} , respectively. Overall, the standard deviation values in Fig. 5 exhibit reasonable distributions, consistent with the results in Table 5.

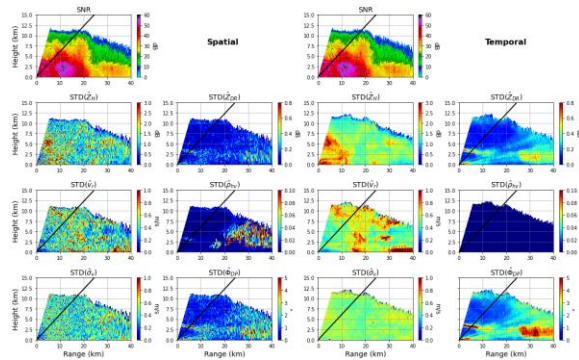


Figure 5. Spatial distribution of SNR, and standard deviations of reflectivity (Z_H), radial velocity (v_r), spectrum width (σ_v), differential reflectivity (Z_{DR}), correlation coefficient (ρ_{hv}), and differential phase shift (Φ_{DP}) for SNR larger than 10 dB from Horus weather observations based on 127 timesteps on 04 October 2023. The first column utilizes 11 spatial gates, and the second column only temporal samples.

(a) Spatial

	$0 \leq \text{SNR}$	$5 \leq \text{SNR} < 10$	$10 \leq \text{SNR} < 15$	$15 \leq \text{SNR} < 20$	$20 \leq \text{SNR}$	Theory	NOAA/NWS RFR
Z_H (dBZ)	1.31	0.62	0.87	0.63	1.31	1.31	1.8
v_r (m/s)	0.41	0.43	0.39	0.31	0.39	0.46	1.0
σ_v (m/s)	0.41	0.53	0.38	0.30	0.39	0.31	1.0
Z_{DR} (dB)	0.09	0.12	0.08	0.06	0.08	0.17	0.3
ρ_{hv}	0.002	0.014	0.006	0.002	0.001	0.001	0.006
Φ_{DP} ($^\circ$)	0.93	1.33	0.92	0.65	0.84	1.11	2.0

(b) Temporal

	$0 \leq \text{SNR}$	$5 \leq \text{SNR} < 10$	$10 \leq \text{SNR} < 15$	$15 \leq \text{SNR} < 20$	$20 \leq \text{SNR}$	Theory	NOAA/NWS RFR
Z_H (dBZ)	1.74	0.94	1.00	0.98	1.82	1.31	1.8
v_r (m/s)	0.53	0.74	0.59	0.57	0.51	0.46	1.0
σ_v (m/s)	0.54	0.81	0.54	0.46	0.52	0.31	1.0
Z_{DR} (dB)	0.20	0.34	0.23	0.16	0.17	0.17	0.3
ρ_{hv}	0.005	0.030	0.015	0.006	0.003	0.001	0.006
Φ_{DP} ($^\circ$)	1.68	3.08	2.07	1.51	1.40	1.11	2.0

Table 5. The standard deviation of six moments based on (a) the spatial and (b) the temporal domain of the Horus data for five different signal-to-noise ratio (SNR) ranges. The NOAA/NWS RFR represent the radar functional requirements of the NOAA and National Weather Service.

4. SUMMARY

There are several limitations in this study, such as (1) differences in the sampling volumes (location and resolution) between the measurements from the operational, dish-based KTLX radar and two stages of development of Horus and (2) assumptions regarding the absolute calibration of the polarimetric variables from KTLX. Although this study has such limitations and could not make use of observations of the same event from co-located radars using the same scanning strategies, it still provides valuable insights into weather observations by assessing the weather measurements from a proposed rotating planar configuration (NOAA 2023).

The standard deviation and mean differences of Horus with 5-panels and 13-panels and two scanning strategies were compared with a collocated operational radar. Despite the differences in filters and averaging processes on the weather measurements, the standard deviations of the radar variables from both PPAR configurations agree well with theoretical expectations and fit within the NOAA/NWS RFR for the cases examined. The standard deviations based on temporal samples are similar or slightly larger than

those from spatial samples and provide more reasonable estimate with the theoretical values. Bias calculations with respect to KTLX reveal biases of -3.44 dB for Z_H , 0.96 dB for Z_{DR} , and -0.003 for ρ_{hv} for the 5-panel configuration, and 5.45 dB for Z_H , 0.25 dB for Z_{DR} and -0.009 for ρ_{hv} from the 13-panel configuration. Although further advancements in the PPAR's design and calibration methods are in progress, this study presents the first quantitative error analysis of 2D PPPAR data. With continuous advances in hardware and software capabilities, Horus exhibits the potential to enhance current operational radars through rapidly updating data with high spatial resolution.

6. Acknowledgements

This work was partially supported by the National Oceanic and Atmospheric Administration (NOAA) under Grant NA16OAR4320115 and the National Science Foundation with the grant of AGS-2136161.

5. REFERENCES

- Cho, J. Y., 2017: A new radio frequency interference filter for weather radars. *Journal of Atmospheric and Oceanic Technology*, **34**, 1393–1406, doi:10.1175/jtech-d-17-0028.1.
- Doviak, R. J., and D. S. Zrnić, 2013: *Doppler radar and weather observations*. Dover publications, New York, NY,.
- Fulton, C., P. Kenworthy, J. Lujan, M. Herndon, S. Garner, D. Thompson, and M. Yearly, 2022: Mutual coupling-based calibration for the Horus Digital Phased Array Radar. *2022 IEEE International Symposium on Phased Array Systems & Technology (PAST)*, doi:10.1109/past49659.2022.9974962.
- Heinselman, P. L., D. L. Prieznitz, K. L. Manross, T. M. Smith, and R. W. Adams, 2008: Rapid sampling of severe storms by the National Weather Radar Testbed Phased Array Radar. *Weather and Forecasting*, **23**, 808–824, doi:10.1175/2008waf2007071.1.
- Ivic, I., C. Curtis, E. Forren, R. Mendoza, D. Schwartzman, S. Torres, D. J. Wasielewski, and F. A. Zahrai, 2019: An overview of weather calibration for the advanced technology demonstrator. *2019 IEEE International Symposium on Phased Array System & Technology (PAST)*, doi:10.1109/past43306.2019.9021053.
- Ivić, I. R., C. Curtis, and S. M. Torres, 2013: Radial-based Noise Power Estimation for weather radars. *Journal of Atmospheric and Oceanic Technology*, **30**, 2737–2753, doi:10.1175/jtech-d-13-00008.1.
- Kollias, P., and Coauthors, 2022: Science applications of phased array radars. *Bulletin of the American Meteorological Society*, **103**, doi:10.1175/bams-d-21-0173.1.
- Kuster, C. M., P. L. Heinselman, and T. J. Schuur, 2016: Rapid-update radar observations of downbursts occurring within an intense multicell thunderstorm on 14 June 2011. *Weather and Forecasting*, **31**, 827–851, doi:10.1175/waf-d-15-0081.1.
- Lei, L., G. Zhang, R. J. Doviak, and S. Karimkashi, 2015: Comparison of theoretical biases in estimating polarimetric properties of precipitation with weather radar using parabolic reflector, or planar and cylindrical arrays. *IEEE Transactions on Geoscience and Remote Sensing*, **53**, 4313–4327, doi:10.1109/tgrs.2015.2395714.
- Li, Z., G. Zhang, M.-H. Golbon-Haghighi, H. Saeidi-Manesh, M. Herndon, and H. Pan, 2021: Initial observations with electronic and mechanical scans using a cylindrical polarimetric phased array radar. *IEEE Geoscience and Remote Sensing Letters*, **18**, 271–275, doi:10.1109/lgrs.2020.2971471.
- Melvin, W. L., 2004: A stap overview. *IEEE Aerospace and Electronic Systems Magazine*, **19**, 19–35, doi:10.1109/maes.2004.1263229.
- National Oceanic and Atmospheric Administration (NOAA), 2023: Report to Congress: Feasibility and Capability of a Rotating Phased Array Radar (.pdf, 816 kB), NOAA report, 19pp.
- Palmer, R. D., and Coauthors, 2023: Horus—a fully digital polarimetric phased array radar for next-generation weather observations. *IEEE Transactions on Radar Systems*, **1**, 96–117, doi:10.1109/trs.2023.3280033.
- Palmer, R., and Coauthors, 2022: A Primer on Phased Array Radar Technology for the Atmospheric Sciences. *Bulletin of the American Meteorological Society*, **103**, doi:10.1175/bams-d-21-0172.1.
- Salazar Aquino, C. M., B. Cheong, and R. D. Palmer, 2021: Progressive Pulse Compression: A novel technique for blind range recovery for solid-state radars. *Journal of Atmospheric and Oceanic Technology*, doi:10.1175/jtech-d-20-0164.1.
- Siggia, A. D. and Passarelli, R. E.: Gaussian model adaptive processing (GMAP) for improved ground clutter cancellation and moment calculation, Proceedings of ERAD, 2004.
- Stailey, J. E., and K. D. Hondl, 2016: Multifunction phased array radar for aircraft and weather surveillance. *Proceedings of the IEEE*, **104**, 649–659, doi:10.1109/jproc.2015.2491179.
- Warde, D., D. Schwartzman, and C. D. Curtis, 2023: Generalized multi-lag estimators (GMLE) for Polarimetric Weather Radar Observations. *IEEE Transactions on Geoscience and Remote Sensing*, **61**, 1–12, doi:10.1109/tgrs.2023.3278489.
- Weber, M., and Coauthors, 2021: Towards the next generation operational meteorological radar. *Bulletin of the American Meteorological Society*, **102**, doi:10.1175/bams-d-20-0067.1.
- Wilson, K. A., P. L. Heinselman, and C. M. Kuster, 2017: Considerations for phased-array radar data use within the National Weather Service. *Weather and Forecasting*, **32**, 1959–1965, doi:10.1175/waf-d-17-0084.1.
- Wirth, W.-D., 2013: *Radar techniques using array antennas*. The Institution of Engineering and Technology, Stevenage, Herts, United Kingdom,.
- Zhang, G., R. J. Doviak, D. S. Zrnić, J. Crain, D. Staiman, and Y. Al-Rashid, 2009: Phased array radar polarimetry for weather sensing: A theoretical formulation for bias corrections. *IEEE Transactions on Geoscience and Remote Sensing*, **47**, 3679–3689, doi:10.1109/tgrs.2009.2029332.
- Zrnić, D. S., and Coauthors, 2007: Agile-beam phased array radar for weather observations. *Bulletin of the American Meteorological Society*, **88**, 1753–1766, doi:10.1175/bams-88-11-1753.
- , R. J. Doviak, D. S. Zrnić, R. Palmer, L. Lei, and Y. Al-Rashid, 2011: Polarimetric phased-array radar for weather measurement: A planar or cylindrical configuration? *Journal of Atmospheric and Oceanic Technology*, **28**, 63–73, doi:10.1175/2010jtecha1470.1.